Effects of Field-Aligned Cold Plasma Density Filaments on the Fine Structure of Chorus

Miroslav Hanzelka[1] and Ondrej Santolik[2]

[1]Institute of Atmospheric Physics (CAS)
[2]Department of Space Physics, Institute of Atmospheric Physics of the Czech Academy of Sciences

November 22, 2022

Abstract

The chorus whistler-mode emission, a major driver of radiation belt electron energization and precipitation, exhibits significant amplitude modulations on millisecond timescales. These subpacket modulations are accompanied by fast changes in the wave normal angle. Understanding the evolution of wave propagation properties inside chorus elements is essential for modeling nonlinear chorus-electron interactions, but the origin of these rapid changes is unclear. We propose that the variations come from propagation inside thin, field-aligned cold plasma enhancements (density ducts), which produce differing modulations in parallel and perpendicular wave magnetic field components. We show that a full-wave simulation on a filamented density background predicts wave vector and amplitude evolution similar to Van Allen Probes spacecraft observations. We further demonstrate that the commonly assumed wide density ducts, in which wave propagation can be studied with ray tracing methods, cannot explain the observed behavior. This indirectly proves the existence of wavelength-scale field-aligned density fluctuations.

Figure 1.

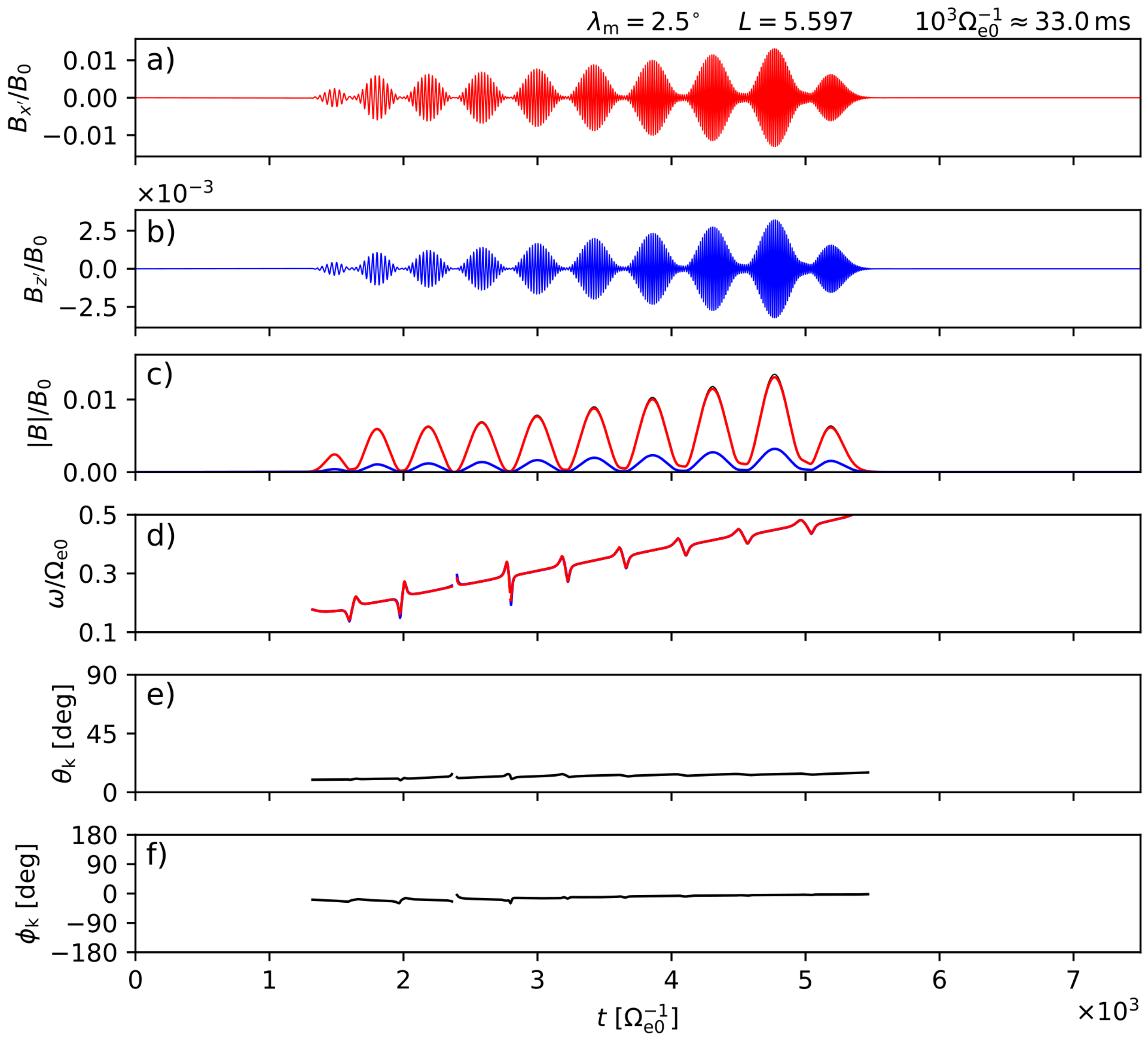

$\lambda_m = 2.5^\circ$
$L = 5.597$
$10^3\Omega_{e0}^{-1} \approx 33.0\,\mathrm{ms}$
a)
$B_{x'}/B_0$
0.01
0.00
−0.01
$\times 10^{-3}$
b)
$B_{z'}/B_0$
2.5
0.0
−2.5
c)
$|B|/B_0$
0.01
0.00
d)
ω/Ω_{e0}
0.5
0.3
0.1
e)
θ_k [deg]
90
45
0
f)
ϕ_k [deg]
180
90
0
−90
−180
0
1
2
3
4
5
6
7
t [Ω_{e0}^{-1}]
$\times 10^3$

Figure 2.

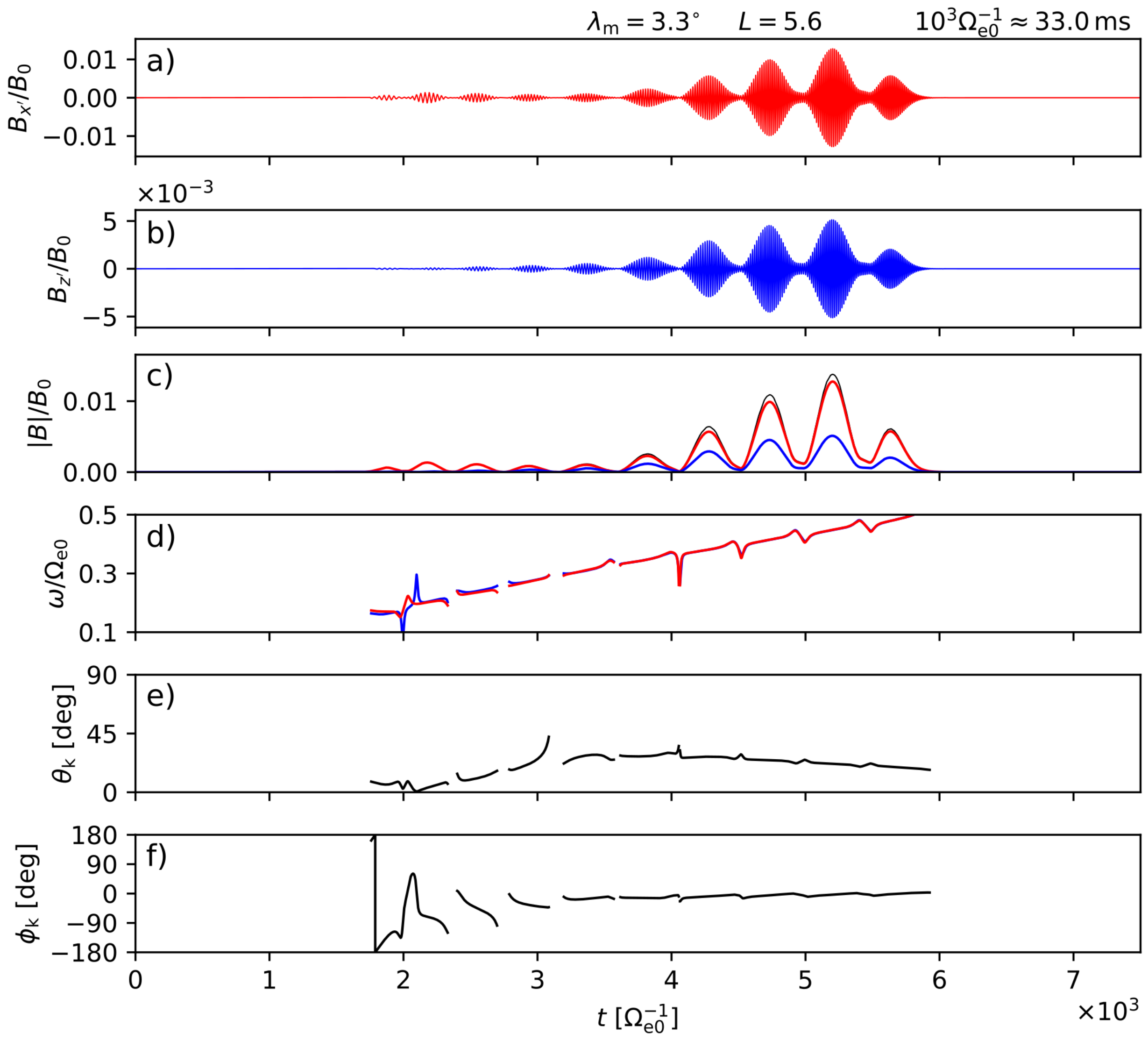

$\lambda_m = 3.3^\circ$
$L = 5.6$
$10^3\Omega_{e0}^{-1} \approx 33.0$ ms
a)
$B_{x'}/B_0$
b)
$\times10^{-3}$
$B_{z'}/B_0$
c)
$|B|/B_0$
d)
ω/Ω_{e0}
e)
θ_k [deg]
f)
ϕ_k [deg]
t [Ω_{e0}^{-1}]
$\times10^3$

Figure 3.

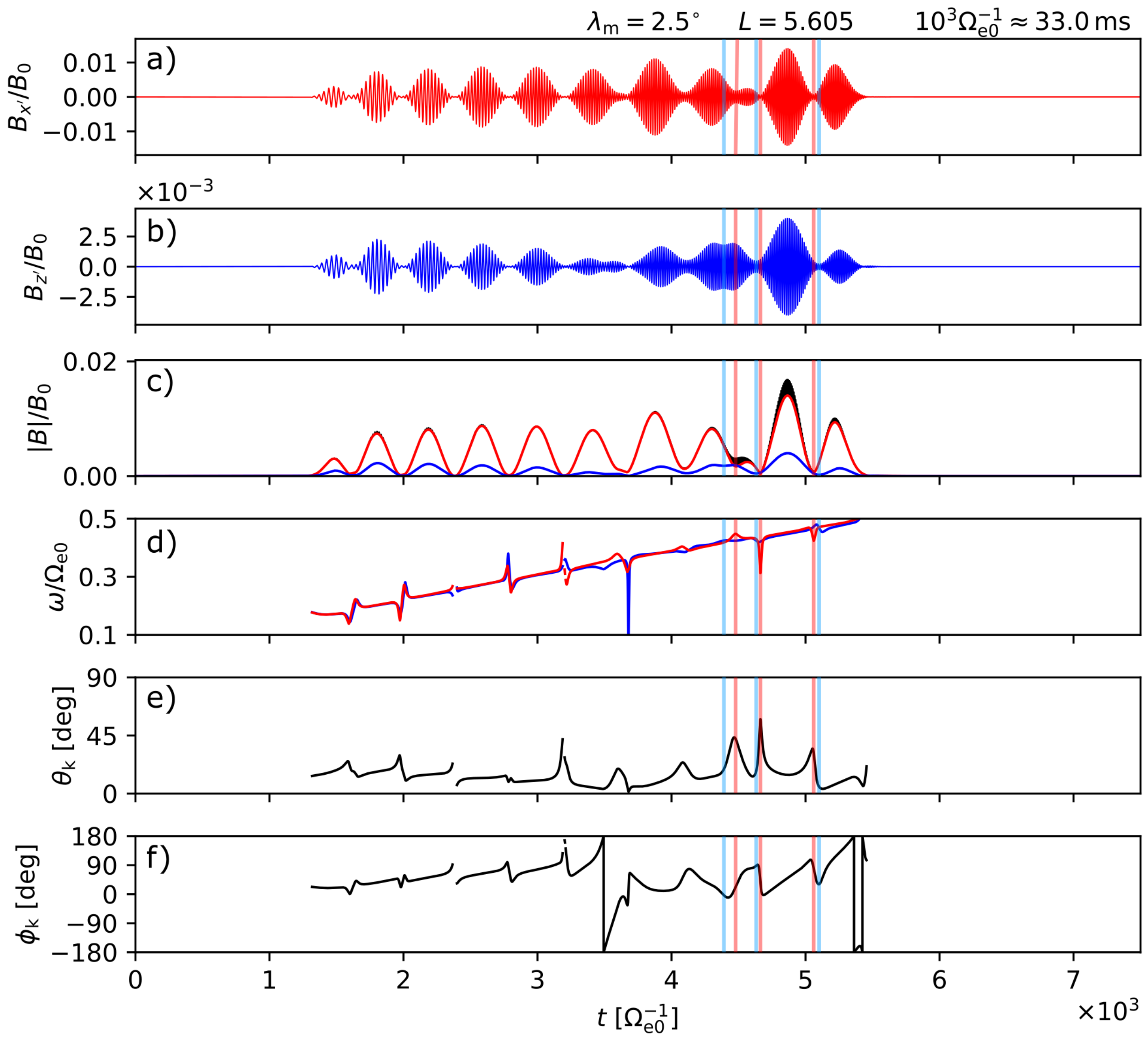

$\lambda_m = 2.5^\circ$
$L = 5.605$
$10^3\Omega_{e0}^{-1} \approx 33.0$ ms
a)
$B_{x'}/B_0$
b)
$\times 10^{-3}$
$B_{z'}/B_0$
c)
$|B|/B_0$
d)
ω/Ω_{e0}
e)
θ_k [deg]
f)
ϕ_k [deg]
t $[\Omega_{e0}^{-1}]$
$\times 10^3$

Figure 4.

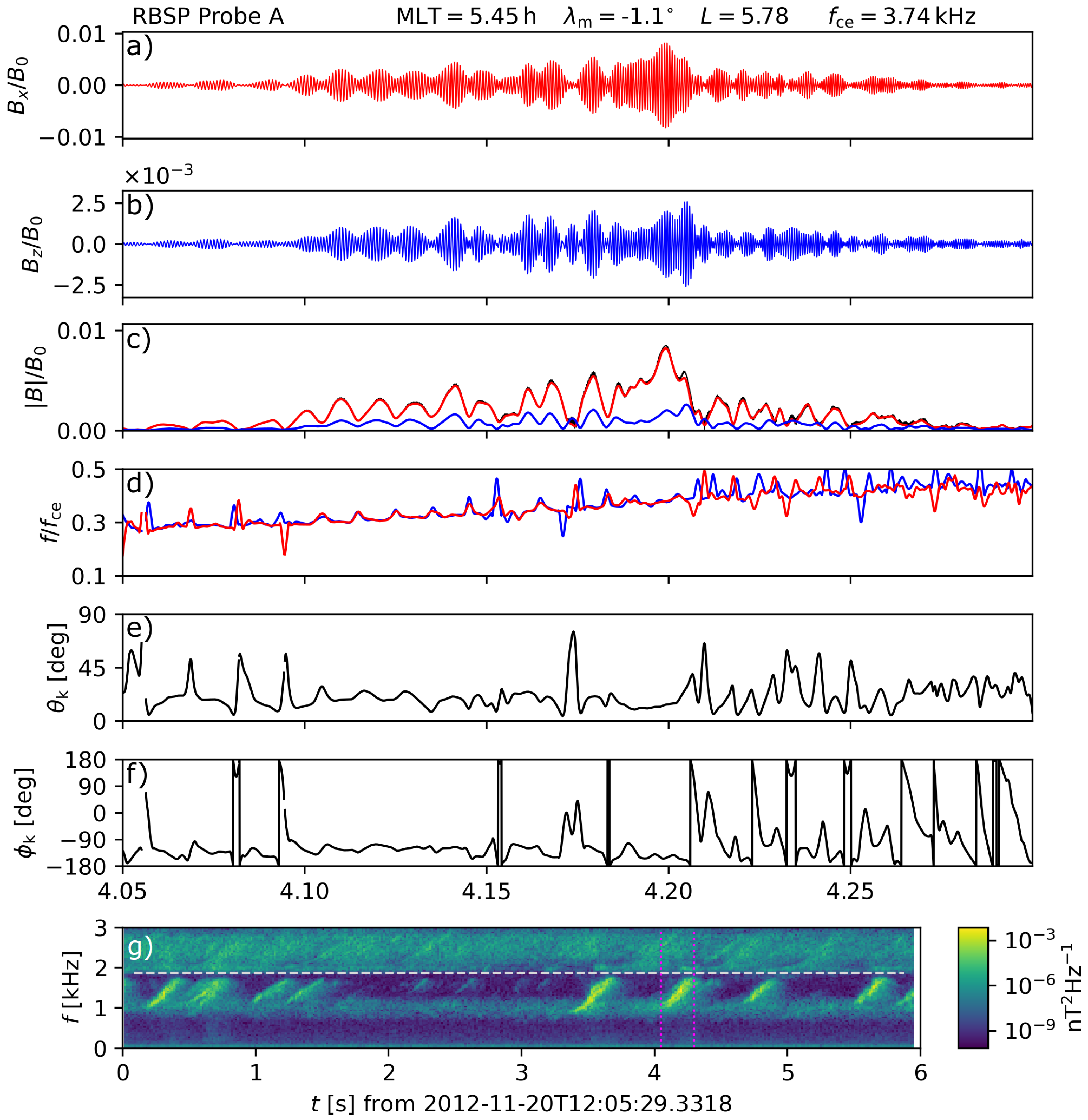

RBSP Probe A
MLT = 5.45 h
λm = -1.1°
L = 5.78
fce = 3.74 kHz
a)
Bx/B0
b)
Bz/B0
×10−3
c)
|B|/B0
d)
f/fce
e)
θk [deg]
f)
ϕk [deg]
g)
f [kHz]
nT2Hz−1
t [s] from 2012-11-20T12:05:29.3318

Effects of Field-Aligned Cold Plasma Density Filaments on the Fine Structure of Chorus

M. Hanzelka[1,2], **O. Santolík**[1,3]

[1]Department of Space Physics, Institute of Atmospheric Physics, Czech Academy of Sciences, Prague, Czech Republic

[2]Center for Space Physics, Boston University, Boston, Massachusetts, USA

[3]Faculty of Mathematics and Physics, Charles University, Prague, Czech Republic

Key Points:

- Propagation of lower-band chorus subpackets near their equatorial source is simulated with finite-difference time-domain methods
- Narrow, field-aligned density enhancement (ducts) create different amplitude modulations in parallel and perpendicular wave components
- Due to the modulation mismatch, instantaneous wave normal angles exhibit rapid variations, matching the behavior observed by spacecraft

Corresponding author: M. Hanzelka, mha@ufa.cas.cz

Abstract

The chorus whistler-mode emission, a major driver of radiation belt electron energization and precipitation, exhibits significant amplitude modulations on millisecond timescales. These subpacket modulations are accompanied by fast changes in the wave normal angle. Understanding the evolution of wave propagation properties inside chorus elements is essential for modeling nonlinear chorus-electron interactions, but the origin of these rapid changes is unclear. We propose that the variations come from propagation inside thin, field-aligned cold plasma enhancements (density ducts), which produce differing modulations in parallel and perpendicular wave magnetic field components. We show that a full-wave simulation on a filamented density background predicts wave vector and amplitude evolution similar to Van Allen Probes spacecraft observations. We further demonstrate that the commonly assumed wide density ducts, in which wave propagation can be studied with ray tracing methods, cannot explain the observed behavior. This indirectly proves the existence of wavelength-scale field-aligned density fluctuations.

Plain Language Summary

The evolution of the Earth's outer radiation belt on short timescales is largely determined by interactions of particles with high-amplitude electromagnetic waves. One type of these electromagnetic emissions, the whistler-mode chorus, exhibits substantial variations in amplitude and propagation direction on the scale of milliseconds. Such rapid changes influence the interaction between the wave and resonant electrons. It is known that the global propagation properties of chorus can be explained by assuming the presence of increases and decreases in plasma density stretched along magnetic field lines (so-called density ducts). We assume the existence of wavelength-scale density ducts and compare two-dimensional solutions of wave equations with chorus signals detected by the Van Allen Probes spacecraft. We demonstrate that, unlike wide ducts, the small-scale irregularities can well explain the observed local wave propagation properties. Our simulations thus indirectly prove the existence of small-scale density fluctuations, which should be accounted for in the analysis of the fine structure of all magnetospheric whistler wave signals.

1 Introduction

The whistler-mode chorus emission (Tsurutani & Smith, 1974; Sazhin & Hayakawa, 1992) is a significant driver of acceleration and scattering of energetic electrons in the Earth's outer radiation belt (Horne et al., 2003; Summers et al., 2007; Lam et al., 2010; Foster et al., 2017). It appears in time-frequency spectrograms as a train of narrowband chirping elements, with each element lasting for hundreds of milliseconds. The power spectrum is often divided by a gap into the lower band, $0.1\Omega_{\mathrm{e0}}$ to $0.5\Omega_{\mathrm{e0}}$ (where Ω_{e0} is the equatorial electron gyrofrequency), and the upper band, $0.5\Omega_{\mathrm{e0}}$ to $0.8\Omega_{\mathrm{e0}}$ (Tsurutani & Smith, 1974; Gao et al., 2019).

Here we focus on the lower-band chorus with a positive chirp rate, the so-called risers. Spacecraft observations have revealed subpacket modulations inside high-amplitude risers (Santolík, Gurnett, et al., 2003), accompanied by irregularities in the instantaneous frequency and the wave vector direction (Santolík et al., 2014). Several simulation studies (Hiraga & Omura, 2020; Zhang et al., 2020; Foster et al., 2021; Hanzelka et al., 2021) have shown that the subpacket structure and fine features of the wave phase evolution influence the efficiency of nonlinear wave-particle interactions. However, there is no consensus on the origin of subpackets, with current models providing only partial explanations (Hanzelka et al., 2020; Tsurutani et al., 2020; Zhang et al., 2020; Tao et al., 2021).

A common aspect of the above-mentioned models is a one-dimensional propagation along magnetic field lines on a smooth cold plasma background. Effects of cold plasma density ducts on the propagation of constant frequency whistler waves have been studied numerically by Streltsov and Bengtson (2020) and Williams and Streltsov (2021) in a homogeneous magnetic field, showing that narrow ducts can lead to the formation of subpackets. Zudin et al. (2019) studied theoretically and numerically the effects of multiple thin ducts on ionospheric whistler waves and discovered that the ducted waves have different dispersive properties than the unducted whistler mode.

Following the results of Hanzelka and Santolík (2019) and Hosseini et al. (2021) on whistler wave propagation in thin, field-aligned density enhancements and lentil-shaped cold plasma irregularities, we propose that the peculiarities of the chorus fine structure come from the dispersion of subpackets in wavelength-scale field-aligned density filaments. We conduct two-dimensional (2D) finite-difference time-domain simulations of a rising-tone chorus propagating in a cold plasma fluid in a dipole magnetic field (Section 2) and study the evolution of wave normal angle θ_{k} and azimuthal angle ϕ_{k} near the equatorial source of parallel waves. The analysis of unducted propagation and effects of both wide and narrow density ducts on magnetic field waveforms (Sections 3.1–3.3), in comparison to Van Allen Probe spacecraft measurements (Section 3.4), lead us to the conclusion that the presence of wavelength-scale density variations is necessary to explain the behavior of wave propagation properties within chorus elements. The impact of these findings on the interpretation of in-situ whistler-mode measurements is discussed in Section 4.

2 Methods

2.1 Wave Simulations

We study the propagation of whistler-mode waves by solving Maxwell's curl equations together with the equations of motion for a cold electron fluid. For our purposes, the linearized fluid motion is sufficient, and after converting velocities to current densities, the equations read

$$\nabla \times \mathbf{B}_{\mathrm{w}} = \mu_0 \mathbf{J} + \frac{1}{c^2}\frac{\partial \mathbf{E}_{\mathrm{w}}}{\partial t}\,, \tag{1}$$

$$\nabla \times \mathbf{E}_{\mathrm{w}} = -\frac{\partial \mathbf{B}_{\mathrm{w}}}{\partial t}\,, \tag{2}$$

$$\frac{\partial(\mu_0 \mathbf{J})}{\partial t} = \frac{\omega_{\mathrm{pe}}^2}{c^2}\mathbf{E}_{\mathrm{w}} - \mu_0 \mathbf{J} \times \frac{e\mathbf{B_0}}{m}\,. \tag{3}$$

The following quantities and notation were used: speed of light c, elementary charge e, electron mass m, vacuum permeability μ_0, time t, electron plasma frequency ω_{pe}, electron current density $\mathbf{J}$, ambient magnetic field $\mathbf{B_0}$, wave magnetic field $\mathbf{B}_{\mathrm{w}}$ ($|\mathbf{B}_{\mathrm{w}}| \ll |\mathbf{B_0}|$), and wave electric field $\mathbf{E}_{\mathrm{w}}$. In all simulation results presented in Section 3, we assume a perfect dipole field $\mathbf{B_0}$ with the strength of $30\,\mu$T at $x = 1R_{\mathrm{E}}$, $z = 0$. Here, R_{E} stands for the Earth's radius, and (x, z) are the solar magnetic (SM) coordinates.

The set of Equations 1-3 is solved by finite difference methods on a 2D staggered Yee grid, a standard approach described, e.g., in Taflove and Hagness (2005). Some recent examples of the application of the FDTD (finite-difference time-domain) method in whistler wave simulations can be found in Katoh (2014) and Hosseini et al. (2021). In our implementation, the simulation box spans from $-30c\Omega_{\mathrm{e0}}^{-1}$ to $350c\Omega_{\mathrm{e0}}^{-1}$ in the z-direction and $x_0 - 50c\Omega_{\mathrm{e0}}^{-1}$ to $x_0 + 40c\Omega_{\mathrm{e0}}^{-1}$ in the x-direction, where $x_0 = 5.6R_{\mathrm{E}}$ is the center of the wave source at $z = 0$. Absorption coefficients are applied to each side of the box to prevent interference with reflected waves. For additional details on the grid parametrization and time stepping, see Text S1 in the Supporting Information (SI).

The chorus element is generated by a cold current source $\mathbf{J}_{\mathrm{s}}(t,x)$ at the equator, defined as

$$\mathbf{J}_{\mathrm{s}}(t,x) = \mathbf{J_0}(t)\cos^2\left(\frac{\pi(x-x_0)}{2w_{\mathrm{J}}}\right) \quad \text{for} \quad |x-x_0| \leq w_{\mathrm{J}}\,, \tag{4}$$

$$\mathbf{J}_{\mathrm{s}}(t,x) = 0 \quad \text{for} \quad |x-x_0| > w_{\mathrm{J}}\,, \tag{5}$$

where w_{J} stands for the halfwidth of the source. Based on the analysis of transverse dimensions of chorus by Santolík and Gurnett (2003), we set $w_{\mathrm{J}} = 150\,\mathrm{km}$. The time-dependent quantity $\mathbf{J_0}(t)$ defines the whistler-mode wave properties:

$$\mathbf{J_0}(t) = J_0 A(t)\,(\cos(\varphi(t)),\,\sin(\varphi(t)),\,0) \quad \text{for} \quad t\in[0,t_{\mathrm{max}}]\,. \tag{6}$$

The z-component of $\mathbf{J_0}$ is explicitly set to zero to model a source of parallel whistler waves. The frequency grows linearly in time with $\omega_0 = \partial\varphi/\partial t(0) = 0.15\Omega_{\mathrm{e0}}$ and $\omega_1 = \partial\varphi/\partial t(t_{\mathrm{max}}) = 0.5\Omega_{\mathrm{e0}}$, $t_{\mathrm{max}} = 4000\Omega_{\mathrm{e0}}^{-1}$. $A(t)$ defines the subpacket modulations, corresponding in our simplified case to 10 subpackets of equal duration from $t=0$ to $t=t_{\mathrm{max}}$, each of them modeled by a $\cos^2(t)$ function. $A(t)$ also defines the ramp-up and fade-out phase of the current, each take $t_{\mathrm{ramp}} = t_{\mathrm{max}}/8$ and are also modeled by a $\cos^2(t)$ function. We keep the amplitude J_0 constant for simplicity; its exact value is unimportant since the equations of motion are linearized and thus do not exhibit nonlinear effects at large wave amplitudes.

The propagation of the modulated whistler-mode wave defined above is studied on three different cold plasma density backgrounds. In the unducted case, we choose a constant density, corresponding to $\omega_{\mathrm{pe0}} = 5\Omega_{\mathrm{e0}}$. In the second case, we investigate the effects of a wide, strong duct, and in the third case, we look at wave propagation in many thin, weak ducts. All ducts have Gaussian profiles and are implemented as

$$n_{\mathrm{e}} = n_{\mathrm{e0}}\left(1-\sum_{i=0}^{N_{\mathrm{d}}}\delta n_i\left(1-\mathrm{e}^{\frac{-(L-L_{\mathrm{d}i})^2}{2\sigma_{\mathrm{L}i}}}\right)\right)\,, \tag{7}$$

where N_{d} is the number of ducts, δn is the relative density change, L_{d} is the central field line, and σ_{L} is the characteristic width of a duct characterized by the standard deviation, with subscript i serving as a duct index. The wide duct is modeled with $N_{\mathrm{d}} = 1$, $\delta n = 0.1$, $L_{\mathrm{d}} = 5.6$ and $\sigma_{\mathrm{L}} = 0.0235$ ($\sim 150\,\mathrm{km}$ at the equator). The thin ducts have a smaller relative density increase and width, $\delta n = 0.03$ and $\sigma_{\mathrm{L}} = 0.00228$ ($\sim 15\,\mathrm{km}$

at the equator), and the centers of adjacent ducts are spaced by $4\sigma_{\mathrm{L}}$; we use $N_{\mathrm{d}} = 19$ thin ducts. Notice that due to the two-dimensionality of our model, the ducts are effectively slabs and not tubes, as they have no dependence on the y-coordinate.

According to the ray tracing results of Hanzelka and Santolík (2019), the density gradients resulting from our choices of δn and σ_{L} should be large enough to guide lower-band whistler waves, but note that the characteristic width of 15 km for thin ducts is comparable to equatorial wavelengths (22 km for $\omega = 0.25\Omega_{\mathrm{e0}}$ and $\theta_{\mathrm{k}} = 0°$), making the approximations of ray optics invalid. This approximation is clearly still valid for the wide duct, which is by one order of magnitude larger. We also conducted numerical tests to confirm that the series of thin ducts is above the threshold discovered by Zudin et al. (2019), under which a comb of narrow density enhancements can be effectively replaced by a smoothed density profile.

The 2D density distributions for the set of thin ducts and for the wide duct are illustrated in Figures S1 and S2 in the Supporting Information, together with examples of simulated spatial distributions of the B_x and B_z components. For comparison, Figure S3 shows an example of these spatial distributions for a case with a homogeneous plasma density without any ducts.

2.2 Signal Analysis

In each simulation, probes were placed inside the box to record time series of the three magnetic field components B_x, B_y, B_z. The position of these probes was defined by a series of magnetic latitudes going from 0.25° to 4.75° with a step of 0.75°, and a series of L-values going from $5.6-2\sigma_{\mathrm{L}}$ to $5.6+2\sigma_{\mathrm{L}}$ with a step of σ_{L} (35 probes in total). In the unducted case, σ_{L} defaults to $1c\Omega_{\mathrm{e0}}^{-1}$ at the magnetic equator. Considering the relatively low velocities of Earth orbiters like the Van Allen Probes (RBSP), whose data are later used for comparison (Section 3.4), the simulation probes were kept stationary. The recorded waveforms of perpendicular and parallel magnetic field components are the primary data product of our simulations.

The time series of the three magnetic field components B_x, B_y, B_z, obtained either from the simulation probes or Van Allen Probes, are first rotated to the field-line coordinate system and then transformed into analytic signals with the Hilbert transform. The magnitude of the analytic signal represents the envelope of each waveform. The instantaneous wave frequency is computed as a numerical derivative (forward difference) of the phase of the signal. In the experimental data, a band-pass filter $0.1\Omega_{\mathrm{e}0} < \omega < 0.49\Omega_{\mathrm{e}0}$ is applied before the transform, and we use the Savitzky-Golay filter to obtain the derivative of phase.

A normalized wave vector $\boldsymbol{\kappa}$ is calculated by the singular value decomposition (SVD) methods described by Santolík, Parrot, and Lefeuvre (2003). The wave normal angle and azimuthal angle are defined as

$$\theta_{\mathrm{k}} = \operatorname{arctan2}(\sqrt{\kappa_{x'}^2 + \kappa_{y'}^2}, \kappa_{z'}) \,, \tag{8}$$

$$\phi_{\mathrm{k}} = \operatorname{arctan2}(\kappa_{y'}, \kappa_{z'}) \,, \tag{9}$$

where the primed coordinates signify the field-aligned system (z' points along the local field line, y' points eastward, and x' completes an orthogonal, right-handed system). Under this definition, $\phi_{\mathrm{k}} = 0°$ means outward propagation, and θ_{k} is always positive.

3 Results

3.1 Unducted Propagation

In the unducted case, we choose the probe at $\lambda_{\mathrm{m}} = 2.5°$, $L = 5.6 - 2\sigma_{\mathrm{L}}$, which corresponds to $\overline{x} = -12.20c\Omega_{\mathrm{e}0}^{-1}$, $z = 155.58c\Omega_{\mathrm{e}0}^{-1}$, where we defined $\overline{x} \equiv x - x_0$. The simulation runs with the wave and background parameters given in Section 2.1 and stops when the last subpacket reaches box boundaries.

In Figures 1a-b, we present the $B_{x'}$, $B_{z'}$ magnetic waveforms recorded by the probe. The increase in amplitude with each subpacket is caused partially by the constant value of J_0 across all frequencies but primarily by the decreasing angle between $\mathbf{B_0}$ and the group velocity, leading to different propagation paths for each packet (note that the first and the last subpacket are strongly affected by the ramp-up of the current). Another dispersion effect is seen at frequencies above $\Omega_{\mathrm{e}}/4$, where the group velocity of a subpacket is larger than the group velocity of the following one. As a result, packets start overlapping, pulling the local minima up to nonzero values – this is best seen on the amplitude envelopes in Figure 1c.

The instantaneous frequency (Figure 1d) exhibits a linear trend, with almost no difference between the perpendicular and the parallel waveform components. Between adjacent subpackets, small ripples appear, with short intervals of negative chirp rates.

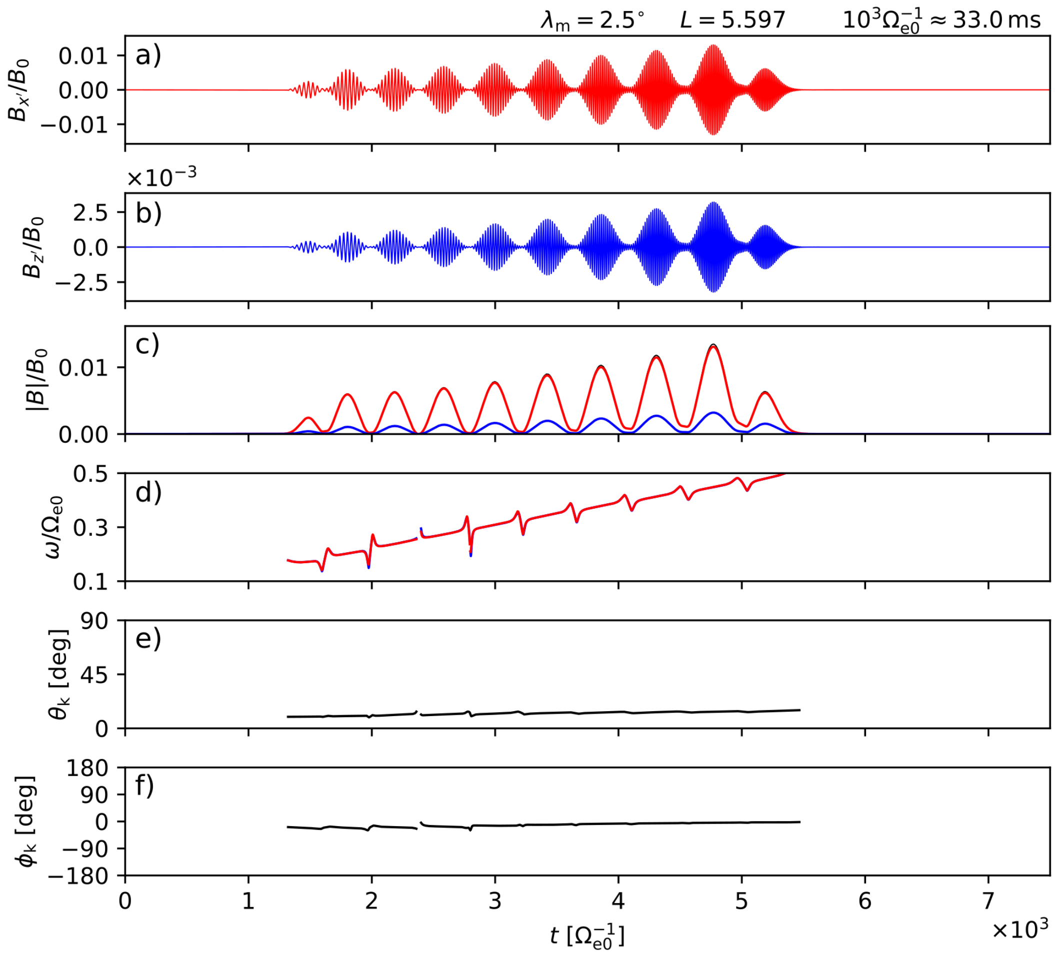

Figure 1. Simulated unducted propagation of a lower-band chorus riser with a subpacket structure. a,b) Waveforms of the perpendicular (red) and parallel (blue) magnetic field components recorded by a probe positioned at $\lambda_m = 2.5^\circ$, $L = 5.597$. c) Amplitude envelopes of the two components from previous panels (red and blue lines) and the total magnetic field (black line). d) Instantaneous frequency obtained from the analytic signal. e) Wave normal angle computed with SVD methods. f) Azimuthal angle of the wave vector, obtained with SVD methods. In panels d-f), intervals corresponding to amplitudes below 1% of the maximum are not plotted.

These irregularities look similar to those in the Hanzelka et al. (2020) model of chorus risers, but here, they come from amplitude modulations instead of inherent nonlinear frequency variations in the source. The explanation for this effect can be found through the second-order expansion of the dispersion relation $\omega(\mathbf{k})$ around the average wavenumber (Wait, 1965), which reveals that short pulses will experience significant spreading in the time domain during propagation in dispersive media. As a result, the edges of initially separate packets start overlapping, leading to phase jumps and associated frequency irregularities. Notice that for $\omega < \Omega_\mathrm{e}/4$, the frequency ripple has an down-up-down form, and for $\omega > \Omega_\mathrm{e}/4$, it changes to up-down-up. This is because for quasiparallel whistler waves, the derivative of V_g with respect to ω changes its sign at $\Omega_\mathrm{e}/4$. These features could change if the phase discontinuities were already present in the source, as in one of the models studied by Zhang et al. (2020).

Another deviation from the constant positive chirp rate can be found inside the first subpacket, which appears to have a nearly constant frequency. This is again a second-order propagation effect, which causes chirping of short pulses in dispersive media. Whistler pulses with $\omega > \Omega_\mathrm{e}/4$ gain a positive chirp, which combines with the frequency growth present in the source. For $\omega < \Omega_\mathrm{e}/4$, we get a negative chirp rate, which explains the suppression of frequency growth at the beginning of the chorus element.

The wave normal angle in Figure 1e rises from 10° to 18°, with negligible fluctuations near the amplitude minima. These values are consistent with our knowledge about the unducted propagation of whistler waves (Breuillard et al., 2012; Hanzelka & Santolík, 2019). The azimuthal angle ϕ_k (Figure 1f) deviates from the outward direction by less than 30° across all frequencies. Overall, the propagation properties of unducted chorus subpackets do not exhibit any unexpected behavior.

3.2 A Single Wide Duct

The second simulation shows the propagation of a chorus element in a single duct with a large width and density variation ($\sigma_\mathrm{L} = 0.0235$, $\delta n = 0.1$). The probe is placed at $\lambda_\mathrm{m} = 3.25°$, $L = 5.6$ (i.e., exactly at the central field line), which corresponds to $\overline{x} = -17.23c\Omega_{\mathrm{e}0}^{-1}$ and $z = 202.06c\Omega_{\mathrm{e}0}^{-1}$. The latitudinal placement was changed from the unducted scenario in Section 3.1 to show some of the behavior related to wave fo-

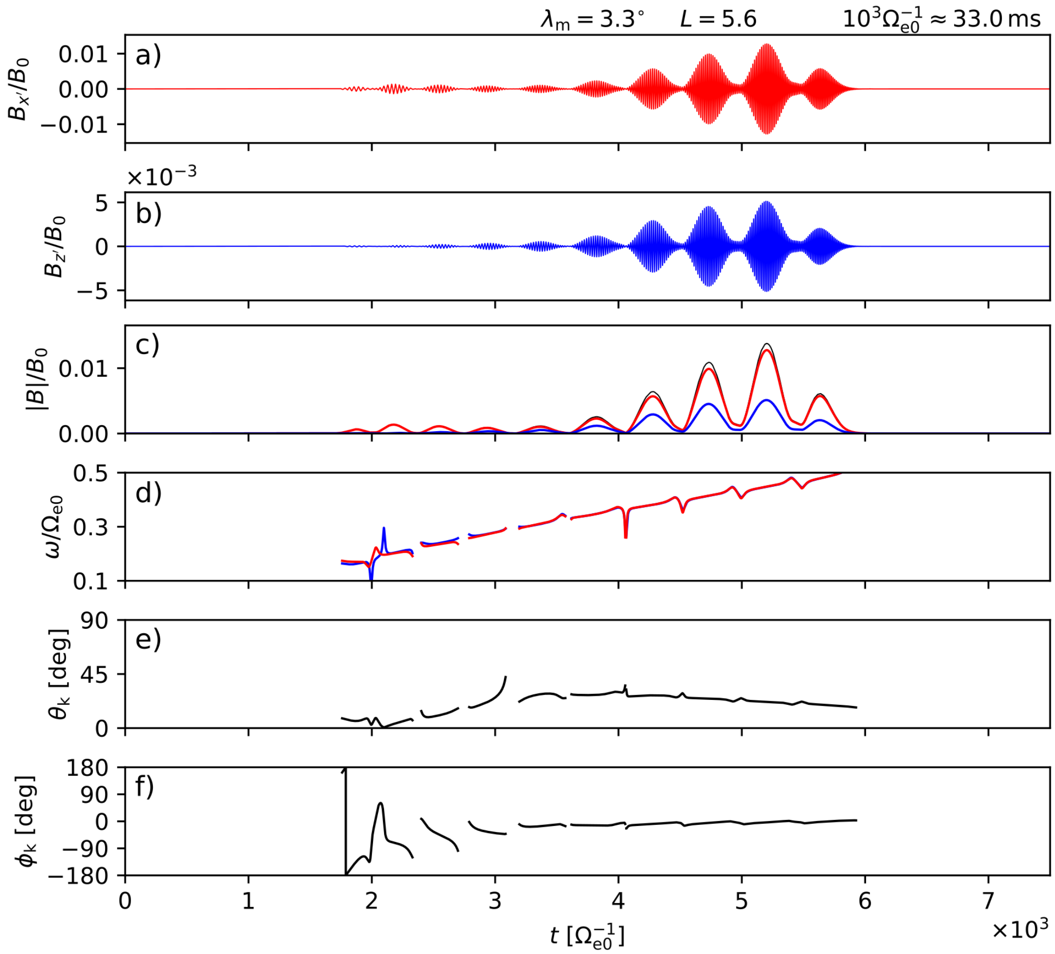

Figure 2. Simulated ducted propagation of a lower-band chorus riser with a subpacket structure. The panel format is the same as in Figure 1. The probe was placed at $\lambda_m = 3.25°$ and $L = 5.6$.

cusation in ducts – see Figure S2 in the SI for placement of the probe within a wavefield snapshot.

Figure 2 shows the waveforms and wave properties in the same format as Figure 1. Because the packets are now focused by the duct and each frequency reflects at a different distance from the central field line, the low-frequency part of the element appears to have amplitudes about an order of magnitude smaller than the maximum. As in the unducted case, higher frequency packets exhibit slight overlaps. The amplitude modulation of the two waveforms is slightly mismatched at the beginning of the element, which manifests in the different frequency behavior of each component in the first two subpackets (Fig. 2c-d).

Another consequence of the $B_{x'}$–$B_{z'}$ envelope mismatch is the larger variations in wave normal angle (Fig. 2e); nevertheless, there is a clear rising trend, followed by a gradual decrease. The azimuthal angles (Fig. 2f) vary wildly in the weaker, low-frequency portion of the element, switching from outward to inward propagation. As the element evolves, the values of ϕ_{k} converge to zero degrees.

3.3 Multiple Thin Ducts

The third and last simulation follows the propagation of a chorus element in a comb of weak and narrow ducts ($\delta n = 0.03$, $\sigma_{\mathrm{L}} = 0.00228$). The probe is positioned at $\lambda_{\mathrm{m}} = 2.5°$, $L = 5.6 + 2\sigma_{\mathrm{L}}$, corresponding to $\overline{x} = -7.31c\Omega_{\mathrm{e0}}^{-1}$ and $z = 155.80c\Omega_{\mathrm{e0}}^{-1}$.

The perpendicular and parallel magnetic field waveforms in Figures 3a-b now differ significantly, especially towards higher frequencies, where additional subpackets appear. This is partially due to the group velocity dispersion, as already discussed in the unducted case, but also due to the spatial variation of amplitude caused by splitting of subpackets by the density filaments (compare with Figure S1). The total magnetic field in Figure 3c starts to oscillate toward the end of the element, suggesting a significant deviation from circular polarization. As in the case of a single duct, the frequencies of $B_{x'}$ and $B_{z'}$ (Fig. 3d) do not exactly match, especially in the time intervals around amplitude minima.

The evolution of wave normal angle in Figure 3e shows rapid variations from 0° up to about 60°, with no clear trend to the average $\theta_{\mathrm{k}}(t)$ across the element. The prominent peaks in θ_{k} appear when the amplitude of $B_{x'}$ reaches a local minimum of a deep modulation, while the amplitude of $B_{z'}$ stays far away from its local minima. These differences in amplitude modulation of perpendicular and parallel components are apparent towards higher frequencies – the last three pairs of amplitude minima are highlighted in Figure 3 by vertical lines. Similar to θ_{k}, we observe large variations in the azimuthal angle ϕ_{k}, with the outward propagation direction being dominant in the recorded waveform.

3.4 Comparison with Spacecraft Observations

The propagation characteristics retrieved from full-wave simulations are compared to Van Allen Probes observations. As a representative example, we chose a lower-band

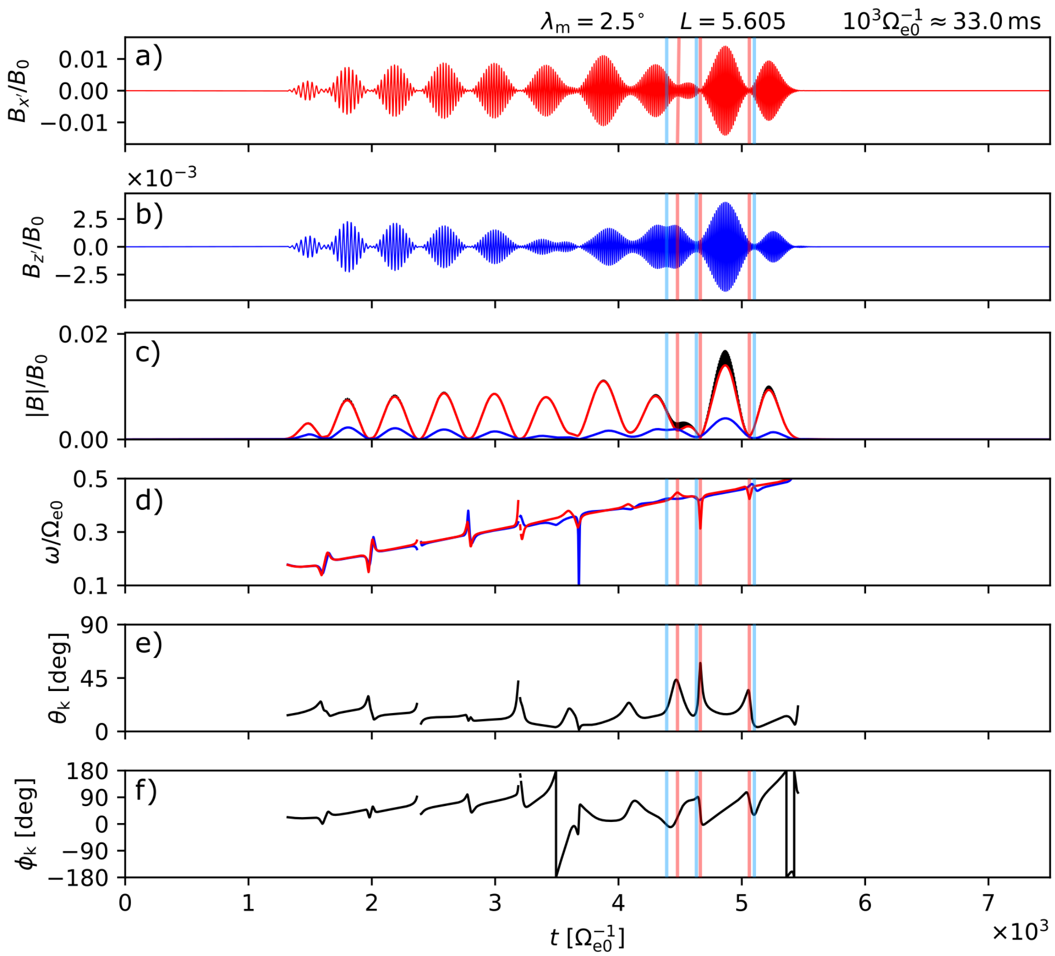

Figure 3. Simulated propagation of a lower-band chorus riser with a subpacket structure on a cold plasma density background modulated by a series of thin ducts. The panel format is the same as in Figure 1, with the addition of red and blue vertical lines, which highlight the amplitude minima of the last three subpackets in the perpendicular and parallel waveforms. The probe was placed at $\lambda_\mathrm{m} = 2.5^\circ$ and $L = 5.605$.

riser observed on 20 November 2012 at 12:05:29.74 UT – 12:05:29.94 UT by the EMFISIS instrument of Probe A. The spacecraft was located at $L = 5.78$, $-1.1°$ of magnetic dipole latitude. The plasma-to-cyclotron frequency ratio was measured to be $\omega_{\mathrm{pe}}/\Omega_{\mathrm{e}} = 5.14$, based on fluxgate data and upper hybrid resonance detection on EMFISIS (Kurth et al., 2015). The frequency of the element ranged from about $0.26\Omega_{\mathrm{e}}$ to $0.47\Omega_{\mathrm{e}}$. The waveforms were recorded with 35 kHz sampling and processed according to Section 2.2. A Savitzky-Golay filter of 3rd order with a window length of 101 points was applied to the amplitude and phase of analytic signals $B_{x'}$ and $B_{z'}$, and the filtered data were then used to obtain the wave properties. The final products are displayed in Figure 4 in the same format as for the simulation results in Figures 1-3.

Looking at $B_{x'}$ and $B_{z'}$ waveforms in Figures 4a-b from $t = 4.095\,\mathrm{s}$ onward, we observe that the subpacket structure matches at lower frequencies, but discrepancies appear as the element evolves. The amplitude modulations also become less regular, with alternating shorter and longer subpackets – this corresponds well to the simulation with many thin ducts. Furthermore, oscillations of the total field (loss of circular polarization) appear in Figure 4c, which is again a feature observed in simulation only when wavelength-scale ducts are present.

The frequency (Fig. 4d) follows a positive linear trend up to about $0.43\Omega_{\mathrm{e}}$ (1.6 kHz), where the growth slows down. The discontinuities between adjacent subpackets have a different character from those in simulations (for $\omega > 0.25\Omega_{\mathrm{e}}$): the up-down-up ripple is replaced by a simpler up-down form, which ends at a higher frequency value than it started. This behavior might come from the more shallow modulations in the experimental data, or it could be related to the apparent lack of chirp inside the subpackets – compare this to the subpacket chirp rate analysis by (Tsurutani et al., 2020). The frequency growth pattern falls apart as the subpacket structure becomes more complex. During the evolution, the mismatch between instantaneous frequencies of $B_{x'}$ and $B_{z'}$ becomes stronger.

The wave normal angle (Fig. 4e) exhibits rapid variations with jumps up to about $60°$, which agrees with the duct-induced patterns displayed in Figure 3e. Based on the behavior of the azimuthal angle in Figure 4f, the propagation direction switches from outward to inward more often than in simulations, especially in the high-frequency part of the element. However, comparing the azimuthal behavior with simulations may be in-

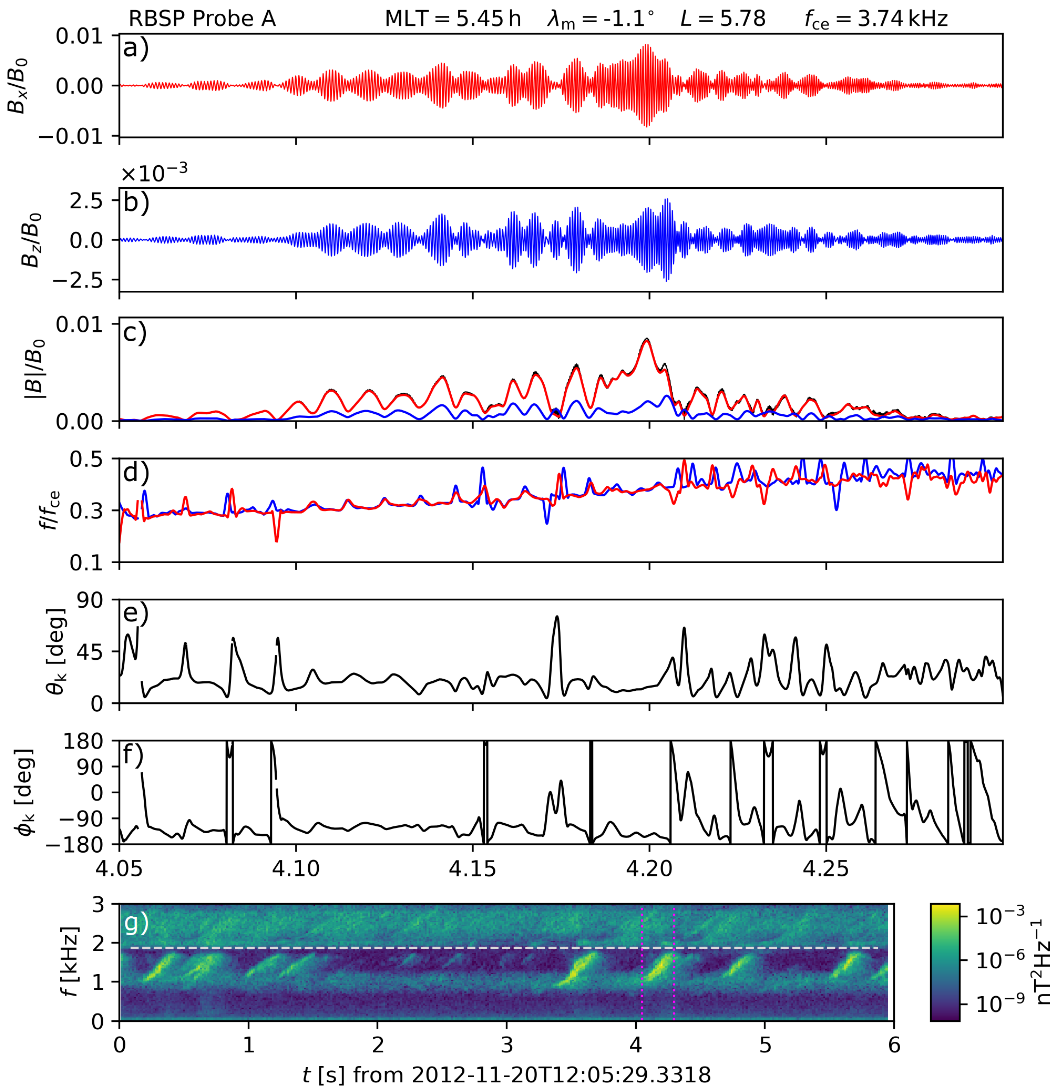

Figure 4. Rising-tone chorus observation made by the EMFISIS instrument on Van Allen Probe A. Panels a-f) show the same type of data as the simulation results in Figure 1, with Savitzky-Golay filter applied on $B_{x'}$ and $B_{z'}$ before processing data for panels d) to f). Panel g) shows an unfiltered spectrogram constructed from a 6-second burst mode snapshot, with the chosen element delimited by dotted magenta lines. The white dashed line represents one half of the gyrofrequency. In panels d-f), intervals corresponding to amplitudes below 1% of the maximum are not plotted.

appropriate, because ducts in the 2D simulation are slab-like structure, unbounded in longitude, while the real ducts are expected to be cylindrical, which was proven in ionospheric environment by Loi et al. (2015). Difference in dispersive properties of 2D and 3D ducted whistler modes was shown theoretically by Zudin et al. (2019).

Overall, we conclude that the experimentally observed patterns in subpacket modulations and wave propagation properties are best explained by the presence of many thin ducts as opposed to a single wide duct or unducted propagation.

4 Discussion and Conclusion

The waveforms shown in Section 3 were recorded at a few fixed points in space, chosen to be about 1500–2000 km from the equatorial source. However, the chorus emissions have a drifting source that can move thousands of kilometers upstream within a single element (Santolík et al., 2004; Demekhov, Taubenschuss, et al., 2020; Nogi & Omura, 2022). It is therefore difficult to estimate how far from the source did Van Allen Probes detect the emission, and how much the waveform could have been affected by propagation effects. Presumably, the high-frequency tail of a chorus element should be affected by propagation more strongly, which is corroborated by the case presented in Figure 4. Comparing simulations to in-situ data obtained too close to the source should be avoided because of the overlap of counter-streaming elements, unless we manage to separate them with an empirical mode decomposition method like the Hilbert-Huang transform (Huang & Wu, 2008). Another caveat is the determination of wave propagation properties near amplitude minima. In our example from Figure 4, peaks in θ_k typically appear when the total amplitude is significant, but in a general case, the narrow hiss band from which the spectral elements grow could interfere with the propagation analysis.

According to our thin-duct propagation hypothesis, the subpacket modulations and θ_k and ϕ_k behavior should become less regular as we go further from the source, especially at higher frequencies. That the few first subpackets can be more regular has already been shown by Santolík, Gurnett, et al. (2003), Crabtree et al. (2017) and Foster et al. (2021), but a statistical analysis is needed. Additionally, the thin duct structure will cause varying amplitude modulations when measuring at multiple points at a fixed latitude but different field lines – Figures S4 and S5 in the Supporting Information show that a few tens of kilometers are enough to completely change the subpacket structure.

This behavior agrees with the multipoint Cluster spacecraft observations of Santolík, Gurnett, et al. (2003) but needs to be confirmed by a more extensive analysis, both numerical and experimental.

An interesting but not surprising feature of the waveforms from Figure 3 are the 2ω-oscillations of the total magnetic field, corresponding to elongation of the polarization ellipse. According to the homogeneous cold plasma dispersion relation (Stix, 1992), the ratio of semi-major to semi-minor axis in the lower frequency band of chorus should not deviate from unity by more than about 1%. However, our plasma is strongly inhomogenous, and the well-known dispersion relation for whistler waves cannot be applied. The detection of similar magnetic field oscillations by Van Allen Probes (Fig. 4c here and Fig. 3c in Santolík et al. (2014)) is another piece of evidence supporting our thin-duct hypothesis and will be analyzed in more detail in our future investigations.

A natural question following our propagation analysis concerns with the origin of the assumed density filamentations. According to the simplified calculations presented by Weibel (1977), the ponderomotive force of high-amplitude whistler waves should have a radial component that forces electrons to move up the amplitude gradient, creating thus the hypothesized ducts. Laboratory experiments by Stenzel (1976) and their theoretical analysis by Sodha and Tripathi (1977) corroborate the tendency of strong whistler waves to self-focus through the formation of density filaments. A more advanced theoretical model of self-channeling and amplitude modulation based on the nonlinear Schrödinger equation was developed by Eliasson and Shukla (2004). However, as far as we know, there has been no first-principle numerical study confirming this behavior, and the expected density modulations are too weak and narrow to be detected in-situ by spacecraft. The results of Yearby et al. (2011) obtained from the Cluster spacecraft potential show localized density enhancements and depletion, but the presence of strong whistler waves puts the validity of the potential method into question.

Finally, we must emphasize that wide ducts (as the one assumed in Section 3.2) are undoubtedly present in the inner magnetosphere and play a major role in the global properties of whistler waves (Demekhov, Titova, et al., 2020; Artemyev et al., 2021; Chen et al., 2021). However, when inspecting the fine structure of chorus, we need to consider the presence of narrow ducts as well, as they provide a simple and convincing explanation for the behavior of wave propagation properties and amplitude modulations on millisecond timescales. Effects of such density irregularities might be difficult to separate from nonlinear growth effects predicted by one-dimensional chorus theories (Tao et al., 2020; Omura, 2021; Zonca et al., 2021). This difficulty cannot be overcome even with 2D PIC simulation (e.g., Ke et al. (2017)) because they treat consistently only the hot electrons and not the cold population. These limitations should be kept in mind during any future attempts to explain the subpacket structure of chorus with nonlinear growth theories.

5 Open Research

The Van Allen Probe data are publicly available from the NASA's Space Physics Data Facility, repository `https://spdf.gsfc.nasa.gov/pub/data/rbsp/`. The FDTD simulation Python code, resulting time series data and processing and plotting routines can be downloaded from `https://doi.org/10.6084/m9.figshare.20319063`.

Acknowledgments

This work has received funding from the European Union's Horizon 2020 research and innovation programme under grant agreement No. 870452 (PAGER).

References

Artemyev, A. V., Demekhov, A. G., Zhang, X. J., Angelopoulos, V., Mourenas, D., Fedorenko, Y. V., ... Shinohara, I. (2021, November). Role of Ducting in Relativistic Electron Loss by Whistler-Mode Wave Scattering. *J. Geophys. Res. Space Physics*, *126*(11), e29851. doi: 10.1029/2021JA029851

Breuillard, H., Zaliznyak, Y., Krasnoselskikh, V., Agapitov, O., Artemyev, A., & Rolland, G. (2012, August). Chorus wave-normal statistics in the Earth's radiation belts from ray tracing technique. *Ann. Geophys.*, *30*(8), 1223-1233. doi: 10.5194/angeo-30-1223-2012

Chen, R., Gao, X., Lu, Q., Chen, L., Tsurutani, B. T., Li, W., ... Wang, S. (2021, April). In Situ Observations of Whistler Mode Chorus Waves Guided by Density Ducts. *J. Geophys. Res. Space Physics*, *126*(4), e28814. doi: 10.1029/2020JA028814

Crabtree, C., Tejero, E., Ganguli, G., Hospodarsky, G. B., & Kletzing, C. A. (2017). Bayesian spectral analysis of chorus subelements from the van allen probes. *J.*

Geophys. Res. Space Physics, *122*(6), 6088-6106. doi: 10.1002/2016JA023547

Demekhov, A. G., Taubenschuss, U., Hanzelka, M., & Santolík, O. (2020, March). Frequency Dependence of Very Low Frequency Chorus Poynting Flux in the Source Region: THEMIS Observations and a Model. *Geophys. Res. Lett.*, *47*(6), e86958. doi: 10.1029/2019GL086958

Demekhov, A. G., Titova, E. E., Maninnen, J., Pasmanik, D. L., Lubchich, A. A., Santolík, O., ... Turunen, T. (2020, May). Localization of the Source of Quasiperiodic VLF Emissions in the Magnetosphere by Using Simultaneous Ground and Space Observations: A Case Study. *J. Geophys. Res. Space Physics*, *125*(5), e27776. doi: 10.1029/2020JA027776

Eliasson, B., & Shukla, P. K. (2004, September). Theoretical and numerical studies of density modulated whistlers. *Geophys. Res. Lett.*, *31*(17), L17802. doi: 10.1029/2004GL020605

Foster, J. C., Erickson, P. J., & Omura, Y. (2021, December). Subpacket structure in strong VLF chorus rising tones: characteristics and consequences for relativistic electron acceleration. *Earth Planets Space*, *73*(1), 140. doi: 10.1186/s40623-021-01467-4

Foster, J. C., Erickson, P. J., Omura, Y., Baker, D. N., Kletzing, C. A., & Claudepierre, S. G. (2017, January). Van Allen Probes observations of prompt MeV radiation belt electron acceleration in nonlinear interactions with VLF chorus. *J. Geophys. Res. Space Physics*, *122*(1), 324-339. doi: 10.1002/2016JA023429

Gao, X., Chen, L., Li, W., Lu, Q., & Wang, S. (2019, April). Statistical Results of the Power Gap Between Lower-Band and Upper-Band Chorus Waves. *Geophys. Res. Lett.*, *46*(8), 4098-4105. doi: 10.1029/2019GL082140

Hanzelka, M., & Santolík, O. (2019, June). Effects of Ducting on Whistler Mode Chorus or Exohiss in the Outer Radiation Belt. *Geophys. Res. Lett.*, *46*(11), 5735-5745. doi: 10.1029/2019GL083115

Hanzelka, M., Santolík, O., Omura, Y., & Kolmašová, I. (2021, September). Measurability of the Nonlinear Response of Electron Distribution Function to Chorus Emissions in the Earth's Radiation Belt. *J. Geophys. Res. Space Physics*, *126*(9), e29624. doi: 10.1029/2021JA029624

Hanzelka, M., Santolík, O., Omura, Y., Kolmašová, I., & Kletzing, C. A. (2020, August). A Model of the Subpacket Structure of Rising Tone Chorus Emissions.

J. Geophys. Res. Space Physics, *125*(8), e28094. doi: 10.1029/2020JA028094

Hiraga, R., & Omura, Y. (2020, February). Acceleration mechanism of radiation belt electrons through interaction with multi-subpacket chorus waves. *Earth Planets Space*, *72*(1), 21. doi: 10.1186/s40623-020-1134-3

Horne, R. B., Glauert, S. A., & Thorne, R. M. (2003, May). Resonant diffusion of radiation belt electrons by whistler-mode chorus. *Geophys. Res. Lett.*, *30*(9), 1493. doi: 10.1029/2003GL016963

Hosseini, P., Agapitov, O., Harid, V., & Gołkowski, M. (2021, March). Evidence of Small Scale Plasma Irregularity Effects on Whistler Mode Chorus Propagation. *Geophys. Res. Lett.*, *48*(5), e92850. doi: 10.1029/2021GL092850

Huang, N. E., & Wu, Z. (2008, June). A review on Hilbert-Huang transform: Method and its applications to geophysical studies. *Rev. Geophys.*, *46*(2), RG2006. doi: 10.1029/2007RG000228

Katoh, Y. (2014, December). A simulation study of the propagation of whistler-mode chorus in the Earth's inner magnetosphere. *Earth Planets Space*, *66*, 6. doi: 10.1186/1880-5981-66-6

Ke, Y., Gao, X., Lu, Q., Wang, X., & Wang, S. (2017, August). Generation of rising-tone chorus in a two-dimensional mirror field by using the general curvilinear PIC code. *J. Geophys. Res. Space Physics*, *122*(8), 8154-8165. doi: 10.1002/2017JA024178

Kurth, W. S., De Pascuale, S., Faden, J. B., Kletzing, C. A., Hospodarsky, G. B., Thaller, S., & Wygant, J. R. (2015, February). Electron densities inferred from plasma wave spectra obtained by the Waves instrument on Van Allen Probes. *J. Geophys. Res. Space Physics*, *120*, 904-914. doi: 10.1002/2014JA020857

Lam, M. M., Horne, R. B., Meredith, N. P., Glauert, S. A., Moffat-Griffin, T., & Green, J. C. (2010, April). Origin of energetic electron precipitation ¿30 keV into the atmosphere. *J. Geophys. Res. Space Physics*, *115*(8), A00F08. doi: 10.1029/2009JA014619

Loi, S. T., Murphy, T., Cairns, I. H., Menk, F. W., Waters, C. L., Erickson, P. J., ... Williams, C. L. (2015, May). Real-time imaging of density ducts between the plasmasphere and ionosphere. *Geophys. Res. Lett.*, *42*, 3707-3714. doi: 10.1002/2015GL063699

Nogi, T., & Omura, Y. (2022, January). Nonlinear Signatures of VLF-Triggered

Emissions: A Simulation Study. *J. Geophys. Res. Space Physics*, *127*(1), e29826. doi: 10.1029/2021JA029826

Omura, Y. (2021, April). Nonlinear wave growth theory of whistler-mode chorus and hiss emissions in the magnetosphere. *Earth Planets Space*, *73*(1), 95. doi: 10.1186/s40623-021-01380-w

Santolík, O., & Gurnett, D. A. (2003, January). Transverse dimensions of chorus in the source region. *Geophys. Res. Lett.*, *30*(2), 1031. doi: 10.1029/2002GL016178

Santolík, O., Gurnett, D. A., Pickett, J. S., Parrot, M., & Cornilleau-Wehrlin, N. (2003, July). Spatio-temporal structure of storm-time chorus. *J. Geophys. Res. Space Physics*, *108*, 1278. doi: 10.1029/2002JA009791

Santolík, O., Gurnett, D. A., Pickett, J. S., Parrot, M., & Cornilleau-Wehrlin, N. (2004, January). A microscopic and nanoscopic view of storm-time chorus on 31 March 2001. *Geophys. Res. Lett.*, *31*(2), L02801. doi: 10.1029/2003GL018757

Santolík, O., Kletzing, C. A., Kurth, W. S., Hospodarsky, G. B., & Bounds, S. R. (2014, January). Fine structure of large-amplitude chorus wave packets. *Geophys. Res. Lett.*, *41*, 293-299. doi: 10.1002/2013GL058889

Santolík, O., Parrot, M., & Lefeuvre, F. (2003, February). Singular value decomposition methods for wave propagation analysis. *Radio Sci.*, *38*, 10-1. doi: 10.1029/2000RS002523

Sazhin, S., & Hayakawa, M. (1992). Magnetospheric chorus emissions: A review. *Planet. Space Sci.*, *40*(5), 681 - 697. doi: https://doi.org/10.1016/0032-0633(92)90009-D

Sodha, M. S., & Tripathi, V. K. (1977, March). Steady-state self-focusing and filamentation of whistlers in a plasma. *J. Appl. Phys.*, *48*(3), 1078-1084. doi: 10.1063/1.323783

Stenzel, R. L. (1976, June). Filamentation instability of a large amplitude whistler wave. *Phys. Fluids*, *19*(6), 865-871. doi: 10.1063/1.861552

Stix, T. (1992). *Waves in Plasmas.* Melville NY: American Institute of Physics.

Streltsov, A. V., & Bengtson, M. T. (2020, October). Observations and Modeling of Whistler Mode Waves in the Magnetospheric Density Ducts. *J. Geophys. Res. Space Physics*, *125*(10), e28398. doi: 10.1029/2020JA028398

Summers, D., Ni, B., & Meredith, N. P. (2007, April). Timescales for radiation belt electron acceleration and loss due to resonant wave-particle interactions: 2. Evaluation for VLF chorus, ELF hiss, and electromagnetic ion cyclotron waves. *J. Geophys. Res. Space Physics*, *112*(A4), A04207. doi: 10.1029/2006JA011993

Taflove, A., & Hagness, S. C. (2005). *Computational Electrodynamics: The Finite-difference Time-domain Method.* Artech House.

Tao, X., Zonca, F., & Chen, L. (2021, September). A "Trap-Release-Amplify" Model of Chorus Waves. *J. Geophys. Res. Space Physics*, *126*(9), e29585. doi: 10.1029/2021JA029585

Tao, X., Zonca, F., Chen, L., & Wu, Y. (2020, January). Theoretical and numerical studies of chorus waves: A review. *Sci. China Earth Sci.*, *63*(1), 78-92. doi: 10.1007/s11430-019-9384-6

Tsurutani, B. T., Chen, R., Gao, X., Lu, Q., Pickett, J. S., Lakhina, G. S., ... Falkowski, B. J. (2020, October). Lower-Band "Monochromatic" Chorus Riser Subelement/Wave Packet Observations. *J. Geophys. Res. Space Physics*, *125*(10), e28090. doi: 10.1029/2020JA028090

Tsurutani, B. T., & Smith, E. J. (1974, January). Postmidnight chorus: A substorm phenomenon. *J. Geophys. Res.*, *79*(1), 118-127. doi: 10.1029/JA079i001p00118

Wait, J. R. (1965). Propagation of pulses in dispersive media. *Radio Sci.*, *69*(11), 1387–1401.

Weibel, E. S. (1977, April). Self channeling of whistler waves. *Phys. Lett. A*, *61*(1), 37-39. doi: 10.1016/0375-9601(77)90256-0

Williams, D. D., & Streltsov, A. V. (2021, December). Determining Parameters of Whistler Waves Trapped in High-Density Ducts. *J. Geophys. Res. Space Physics*, *126*(12), e29228. doi: 10.1029/2021JA029228

Yearby, K. H., Balikhin, M. A., Khotyaintsev, Y. V., Walker, S. N., Krasnoselskikh, V. V., Alleyne, H. S. C. K., & Agapitov, O. (2011, September). Ducted propagation of chorus waves: Cluster observations. *Annales Geophysicae*, *29*(9), 1629-1634. doi: 10.5194/angeo-29-1629-2011

Zhang, X. J., Agapitov, O., Artemyev, A. V., Mourenas, D., Angelopoulos, V., Kurth, W. S., ... Hospodarsky, G. B. (2020, October). Phase Decoherence

Within Intense Chorus Wave Packets Constrains the Efficiency of Nonlinear Resonant Electron Acceleration. *Geophys. Res. Lett.*, *47*(20), e89807. doi: 10.1029/2020GL089807

Zonca, F., Tao, X., & Chen, L. (2021, December). Nonlinear dynamics and phase space transport by chorus emission. *Rev. Mod. Plasma Phys.*, *5*(1), 8. doi: 10.1007/s41614-021-00057-x

Zudin, I. Y., Zaboronkova, T. M., Gushchin, M. E., Aidakina, N. A., Korobkov, S. V., & Krafft, C. (2019, June). Whistler Waves' Propagation in Plasmas With Systems of Small-Scale Density Irregularities: Numerical Simulations and Theory. *J. Geophys. Res. Space Physics*, *124*(6), 4739-4760. doi: 10.1029/2019JA026637

Supporting Information for "Effects of Field-Aligned Cold Plasma Density Filaments on the Fine Structure of Chorus"

M. Hanzelka[1,2], O. Santolík[1,3]

[1]Department of Space Physics, Institute of Atmospheric Physics, Czech Academy of Sciences, Prague, Czech Republic

[2]Center for Space Physics, Boston University, Boston, Massachusetts, USA

[3]Faculty of Mathematics and Physics, Charles University, Prague, Czech Republic

Contents of this file

Introduction

This file contains one short supplementary text describing the parameters of our FDTD simulation scheme, followed by five figures. The first three Figures, S1 to S3, show snapshots of the simulated chorus magnetic wavefield in scenarios with and without ducts. These snapshots help in understanding the propagation paths and attenuation of individual subpackets. The last two figures, S4 and S5, show the waveforms and propagation

---

Corresponding author: M. Hanzelka (mirekhanzelka@gmail.com)

properties of the chorus element propagating through thin ducts. The placement of probes that recorded the waveforms differs from Figure 4 in the main text. These supporting figures confirm the high variability of the subpacket structure in space.

Text S1. Parameters of the finite-difference time-domain scheme.

Unlike Katoh (2014), we limit our investigations to a few degrees of latitude around the magnetic equator, allowing us to use rectilinear coordinates instead of curvilinear without any significant increase in memory demands. The grid size is chosen so that at the equator, across all frequencies of a model wave packet, both parallel and perpendicular wavelengths are resolved by at least 12 points for θ_k going up to 75 % of the local resonance cone $\theta_\mathrm{res}(\omega)$. That is,

$$\Delta z \leq 12 \cdot \frac{2\pi}{k_\parallel(\omega,\theta_\mathrm{k})} \quad \forall\,\omega \in [\omega_0,\omega_1],\, \theta_\mathrm{k} \leq \frac{3}{4}\theta_\mathrm{res}(\omega)\,, \tag{1}$$

$$\Delta x \leq 12 \cdot \frac{2\pi}{k_\perp(\omega,\theta_\mathrm{k})} \quad \forall\,\omega \in [\omega_0,\omega_1],\, \theta_\mathrm{k} \leq \frac{3}{4}\theta_\mathrm{res}(\omega)\,, \tag{2}$$

where $k_\parallel$ and $k_\perp$ are the wave vector components, and ω_0 and ω_1 are the lowest and highest wave frequency. Additionally, the characteristic scale length of transverse density irregularities at the equator (see σ_L in Equation 7 of the main text) must be covered by at least 8 points. We tested various finer grids to confirm that our choice produces negligible numerical errors. Finally, to ensure stability, the time step Δt was chosen as

$$c\Delta t = \frac{1}{1/\Delta x + 1/\Delta z}\,, \tag{3}$$

which results in a free-space CFL-number between $1/\sqrt{2}$ and 1 for any positive $\Delta x/\Delta z$ ratio (Taflove & Hagness, 2005).

References

Katoh, Y. (2014, December). A simulation study of the propagation of whistler-mode chorus in the Earth's inner magnetosphere. *Earth Planets Space*, *66*, 6. doi: 10.1186/1880-5981-66-6

Taflove, A., & Hagness, S. C. (2005). *Computational Electrodynamics: The Finite-difference Time-domain Method.* Artech House.

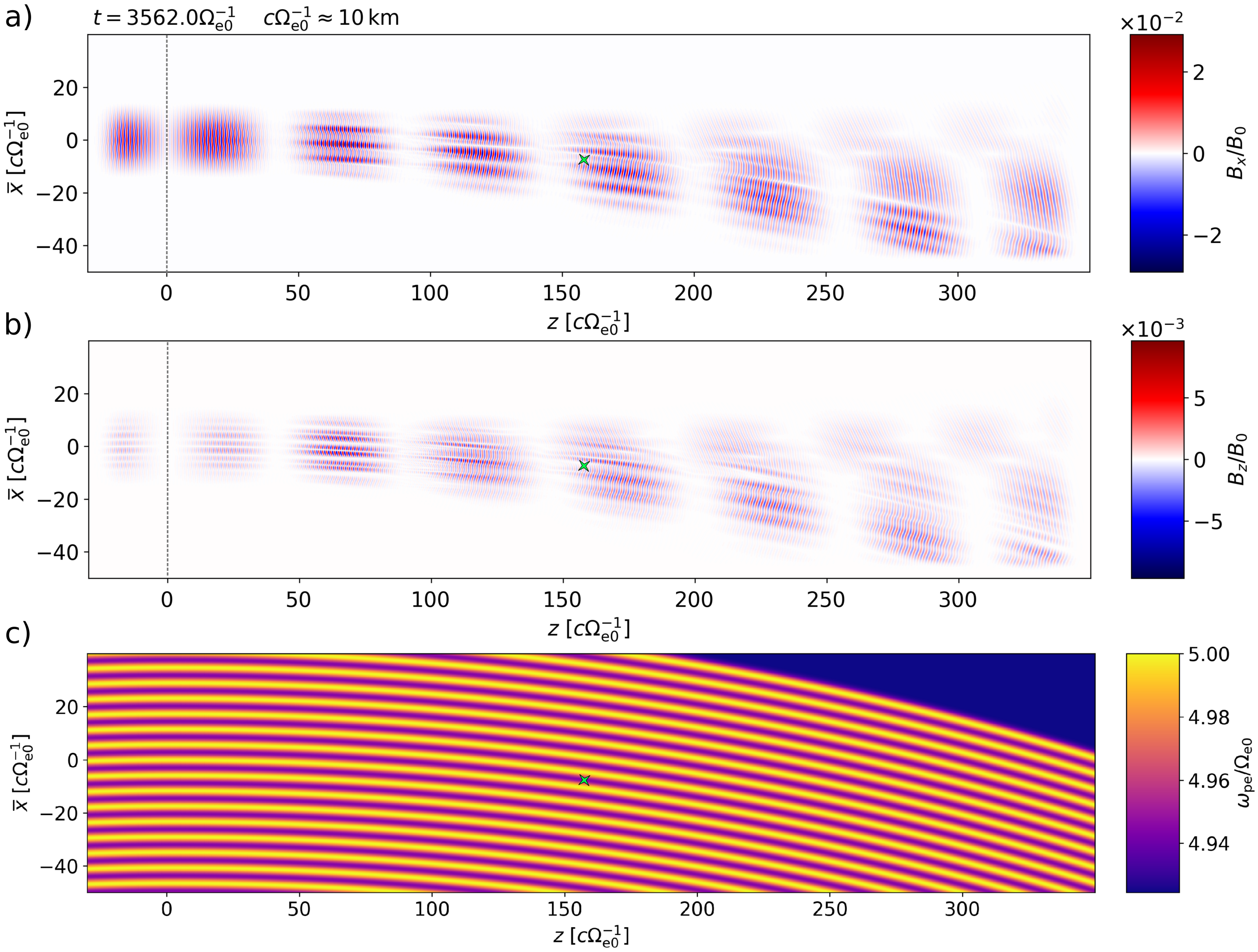

Figure S1. Propagation of chorus subpackets in a series of thin, field-aligned density enhancements. a,b) Magnetic field components B_x, B_z at time $t = 3562\Omega_{e0}^{-1} \approx 120\,\mathrm{ms}$. We observe that the amplitude becomes focused into individual ducts shortly after leaving the source, with part of the wave becoming unducted and escaping at larger distances. The snapshots were taken after the ninth subpacket was generated. c) Electron plasma frequency ω_{pe}. The green stars mark the position of a probe that recorded the waveforms from Figure 3 in the main text.

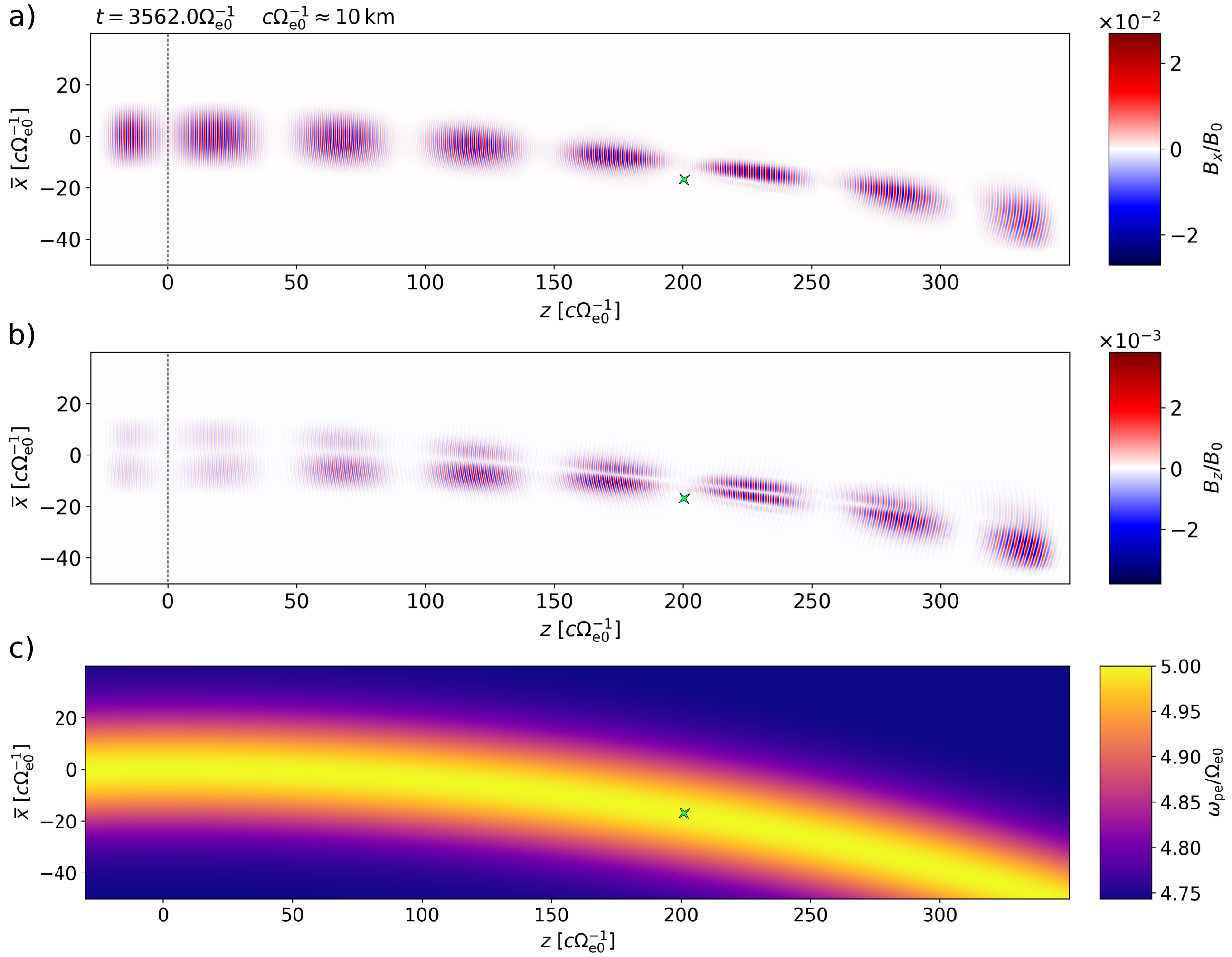

Figure S2. Propagation of chorus subpackets in a wide, field-aligned density enhancement. a,b) Magnetic field components B_x, B_z at time $t = 3562\Omega_{e0}^{-1} \approx 120$ ms, just before the generation of the last (tenth) subpacket. c) Electron plasma frequency ω_{pe}. The green stars mark the position of a probe that recorded the waveforms from Figure 2 in the main text.

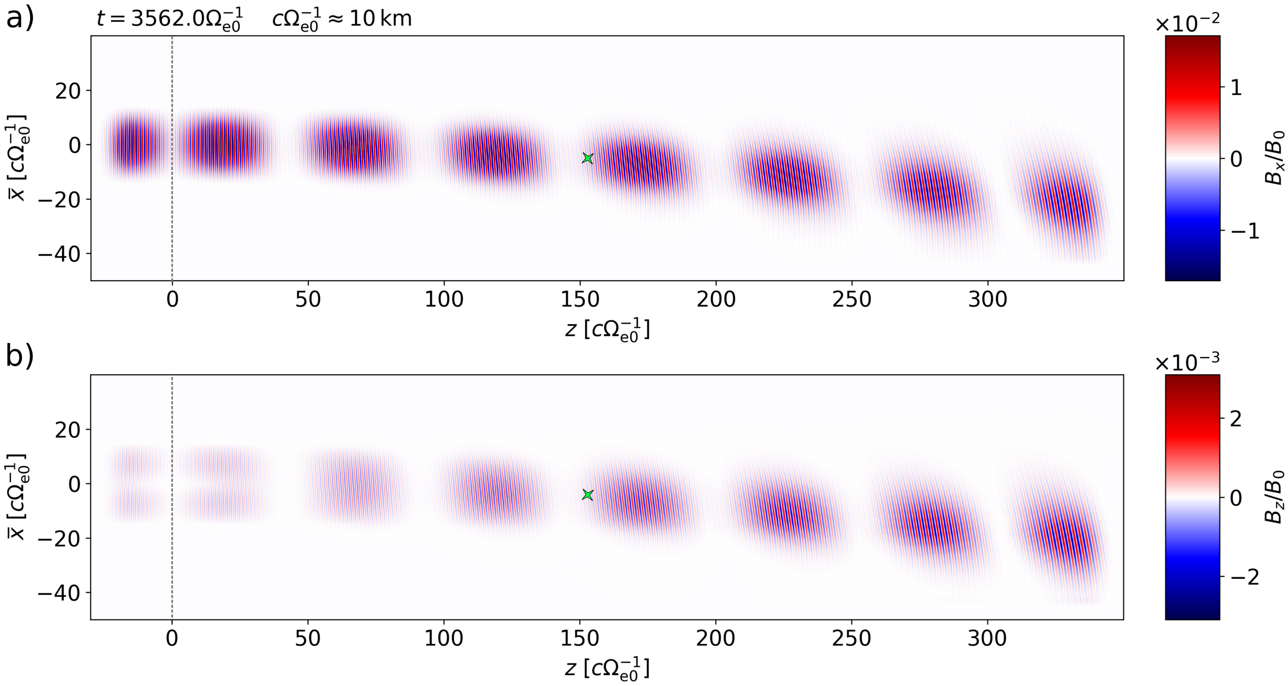

Figure S3. Unducted propagation of chorus subpackets. a,b) Magnetic field components B_x, B_z at time $t = 3562\Omega_{e0}^{-1} \approx 120\,\mathrm{ms}$, just before the generation of the last (tenth) subpacket. The green stars mark the position of a probe that recorded the waveforms from Figure 1 in the main text.

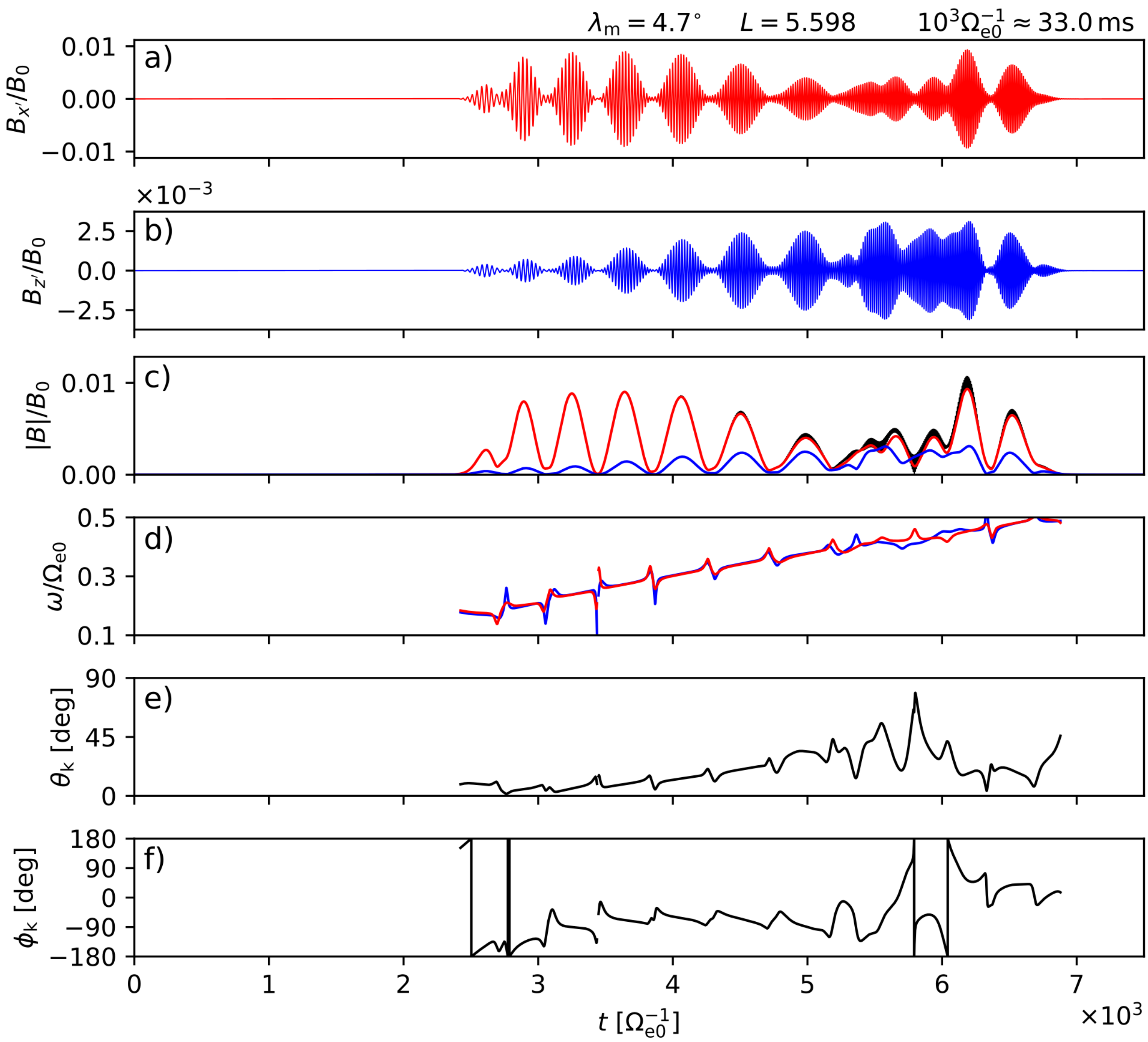

Figure S4. Simulated propagation of a lower-band chorus riser with a subpacket structure on a cold plasma density background modulated by a series of thin ducts. The panel format is the same as in Figure 3 of the main text, but the probe was placed further away from the source at $\lambda_{\mathrm{m}} = 4.75°$ and $L = 5.598$ ($-\sigma_{\mathrm{L}}$ from the central field line).

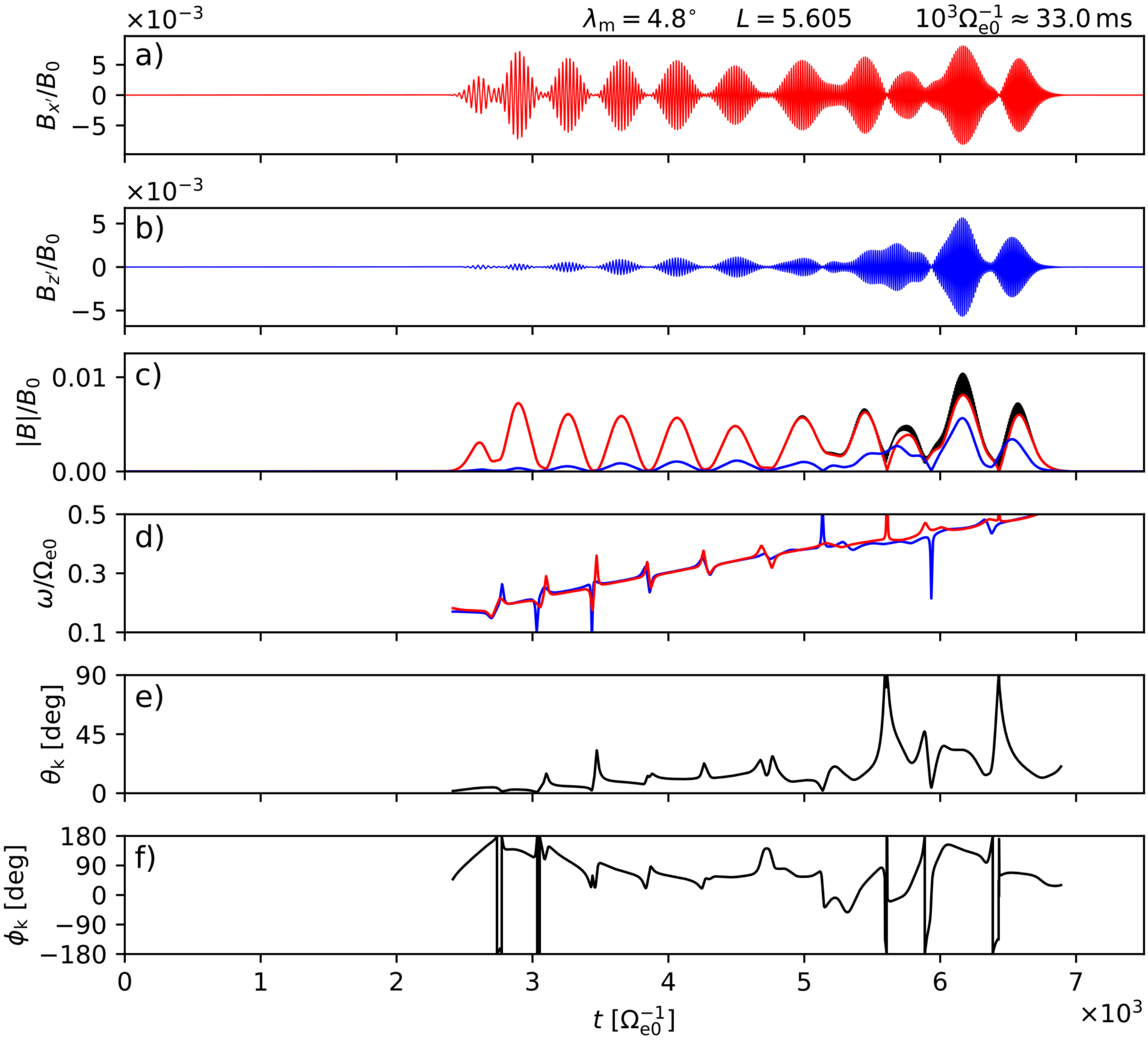

Figure S5. Simulated propagation of a lower-band chorus riser with a subpacket structure on a cold plasma density background modulated by a series of thin ducts. The panel format is the same as in Figure 3 of the main text, but the probe was placed further away from the source at $\lambda_\mathrm{m} = 4.75^\circ$ and $L = 5.605$ ($+2\sigma_\mathrm{L}$ from the central field line). This is the same latitude as in Figure S4, but transverse by position is shifted by $3\sigma_\mathrm{L} \approx 43$km. Notice that the subpacket structures differ significantly, especially at higher frequencies.